



Information theoretic evaluation of Lorentzian, Gaussian, Voigt, and symmetric alpha-stable models of reversible transverse relaxation in cervical cancer in vivo at 3 T

Pelin Ciris¹

Received: 30 May 2022 / Revised: 19 July 2022 / Accepted: 21 July 2022 / Published online: 4 August 2022

© The Author(s), under exclusive licence to European Society for Magnetic Resonance in Medicine and Biology (ESMRMB) 2022

Abstract

Objects To better characterize cervical cancer at 3 T. MRI transverse relaxation patterns hold valuable biophysical information about cellular scale microstructure. Lorentzian modeling is typically used to represent intravoxel frequency distributions, resulting in mono-exponential decay of reversible transverse relaxation. However, deviations from mono-exponential decay are expected theoretically and observed experimentally.

Materials and methods We compared the information content of four models of signal attenuation with reversible transverse relaxation. Biological phantoms and six women with cervical squamous cell carcinoma were imaged using a gradient-echo sampling of the spin-echo (GESSE) sequence. Lorentzian, Gaussian, Voigt, and Symmetric α -Stable (SAS) models were ranked using Akaike's Information Criterion (AIC), and the model retaining the highest information content was identified at each voxel as the best model.

Results The Lorentzian model resulted in information loss in large fractions of the phantoms and cervix. Gaussian and SAS models frequently had higher information content than the Lorentzian in much of the areas of interest. The Voigt model rarely surpassed the three other models in terms of information content.

Discussion Gaussian and SAS models provide better fitting of data in much of the human cervix at 3 T. Minimizing information loss through improved tissue modeling may have important implications for identifying reliable biomarkers of tumor hypoxia and iron deposition.

Keywords Biophysical modeling · Relaxometry · Lorentzian · Gaussian · Cervical cancer

Introduction

Many methods crucial for diagnostic imaging to non-invasive studies of neuroscience, physiology, and biology, rely on the fundamental physical NMR phenomenon of transverse relaxation. Transverse relaxation results from variations, in time or in space, of the magnetic field and can be observed following an initial excitation of spin precession: individual spins experience varying Larmor frequency offsets due to the local magnetic environment and acquire different precession phases (dephase), such that the signal

magnitude, resulting from the vector sum of the contributions from each spin, gradually decreases (FID), or correspondingly, the spectral line broadens (line broadening). While completely uniform fluids undergo some dephasing due to random molecular motion, the spatially heterogeneous environment of biological tissues with varying magnetic susceptibilities [1, 2] additionally contributes to dephasing at the molecular (nanometer), cellular (mesoscopic, micrometer), and macroscopic (MR voxel, millimeter) scales. At MRI temporal resolutions, the Brownian motion and diffusion length of spin carrying molecules is on the order of the cellular scale of structural organization, and the interplay between diffusion and transverse relaxation bestrides two idealized limiting cases: (1) the motional-, or diffusion-narrowing regime, when spins sample sufficiently large portions of a medium during their Brownian motion, their phases will have the same statistical distribution; (2) the static dephasing regime, when spins are static, phase differences between

✉ Pelin Ciris
pelin.aksit@gmail.com

¹ Department of Biomedical Engineering, Faculty of Engineering, Akdeniz University, A305, 07070 Antalya, Türkiye

remote spins will be due to the spatially variable magnetic field [3–5]. The resulting transverse relaxation pattern over time holds valuable biophysical information about cellular scale microstructure.

Signal decay in measurements involving spin echoes (SE) correspond to irreversible transverse relaxation and can differ from measurements involving gradient echoes (GE), which correspond to reversible transverse relaxation. Considering effects of irreversible and reversible transverse relaxation jointly may further improve understanding of the underlying micro-structural complexity [6]. Simultaneous investigation of irreversible and reversible transverse relaxation is possible using pulse sequences such as gradient-echo sampling of the FID and echo (GESFIDE) [7] or gradient-echo sampling of the spin-echo (GESSE) sequences [8]. GESFIDE and GESSE sample signals during dephasing by both irreversible and reversible transverse relaxation, as well as during rephasing by reversible processes working against dephasing by irreversible processes. When reversible transverse relaxation is linear exponential, GESFIDE offers a clear SNR advantage over GESSE, however, if not, then the temporal behavior of the FID and left- and right-hand sides of SEs differ significantly from the expected.

Signal decay with reversible transverse relaxation often appears nearly exponential (especially at longer minimal echo times) and is typically modelled using a corresponding Lorentzian intravoxel frequency distribution (equivalent to a Cauchy distribution). However, this signal decay is not always exponential [4], and the Lorentzian model is a poor approximation since the distribution of metabolites in living tissue are typically not homogeneous, susceptibilities are spatially dependent with a distribution of resonance frequencies [9], resulting in rather non-mono-exponential signal decays [5]. The theoretical expectation that intravoxel precession frequency distribution is sometimes better modeled as non-Lorentzian (i.e., Gaussian) has also been recently supported experimentally, in the brain [10–12], lungs [13], prostate [14] and teeth [15] as well as blood [16].

Fitting spectra with inappropriate line shapes introduces systematic errors in quantification [9, 14]. The Voigt distribution is defined as the convolution of Lorentzian and Gaussian distributions, and has previously been shown to model in vivo MRS resonances better than purely Lorentzian or Gaussian distributions, with considerably smaller residual spectrums [9, 17]. The simplified pseudo-Voigt distribution is the linear combination of Lorentzian and Gaussian distributions, and also performed better than either purely Lorentzian or Gaussian distributions for chemical exchange saturation transfer (CEST) and nuclear Overhauser enhancement (NOE) quantification in mice at 11.7 T [18]. More recently, the Symmetric α -Stable (SAS) distribution was reported to better fit field distributions compared to purely Lorentzian

or Gaussian distributions for many voxels in the brain [10]. Both Voigt and SAS distributions are more generalized line shapes, they have one additional degree of freedom relative to a Lorentzian or Gaussian, and they can reduce to either a Lorentzian or a Gaussian (which are simple subtypes of these more generalized distributions) for certain values of this additional parameter. In other words, both Voigt and SAS can become equivalent to a Lorentzian or a Gaussian or can provide intermediate distributions between a Lorentzian and Gaussian. Such two-parameter descriptions may better quantify the underlying frequency distribution than the linewidth of a poorly fitting Lorentzian. Lorentzian, Gaussian, as well as sample Voigt and SAS distributions are depicted in Fig. 1. The Voigt distribution based on convolution was used in this work (rather than the simplified pseudo-Voigt distribution). More accurate quantification of relaxation may allow for better connections to specific biophysical models of water interactions in tissue that ultimately lead to disparate relaxation patterns, compared to oversimplified relaxation “maps” based on purely Lorentzian distributions with purely exponential decays.

Correct signal characterization is important for establishment of accurate MRI biomarkers. A biomarker for hypoxia, or reduced oxygen tension, in tumors is desirable, and may better guide treatment of hypoxic tumors which tend to have increased metastatic potential, are more resistant to radiation treatment, and result in poor patient outcomes [19–24]. Hypoxia is prevalent among cervical cancers, with up to 48% showing this aggressive phenotype [25], which relative to non-hypoxic tumors increases mortality by two- to

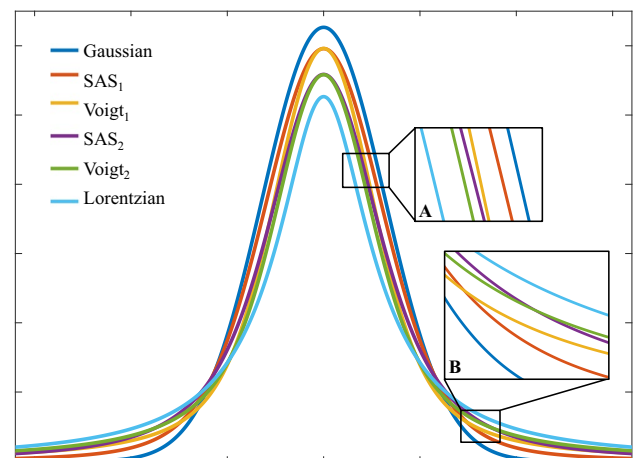


Fig. 1 Lorentzian, Gaussian, Voigt, and SAS distributions. Voigt and SAS distributions are generalized line shapes and can provide intermediate distributions between a Lorentzian and Gaussian or match a Lorentzian or a Gaussian. The distributions are demonstrated for comparison, normalized, using the following parameters: Common: $R_2 = 0.5$, $R_2' = 2$, $\sigma = 2$; Voigt₁: $R_2' = 1.08$, $\sigma = 1.18$; Voigt₂: $R_2' = 1.43$, $\sigma = 0.95$; SAS₁: $\alpha = 1.67$, SAS₂: $\alpha = 1.33$

threefold [26]. Improved targeting of hypoxia in tumors may improve treatment response and survival [27]. To date, efforts at identifying intra-tumoral hypoxia have mainly targeted the effective relaxation of GE signal decays from reversible and irreversible relaxation effects [28–31]. In this work we compared Lorentzian, Gaussian, Voigt, or SAS distributions as models of signal attenuation with reversible transverse relaxation, in terms of information content, on data acquired using GESSE sequences, in biological phantoms and women with cervical cancers, at 3 T. The Voigt distribution has not previously been utilized in this context in MRI, and cervical cancers have not previously been investigated with GESSE or the SAS model. Our findings may help improve tumor characterization in women with cervical cancers at 3 T, with better modeling of (i.e., hypoxia related) susceptibility effects, treatment guidance at baseline, and monitoring following therapy.

Methods

Theory

GESSE sequences facilitate assessment of the effects of intravoxel Larmor frequency distribution, by following the evolution of transverse magnetization at various dephasing states during a SE experiment, both before and after complete rephasing of all components, and by correctly accounting for irreversible relaxation.

Signal magnitude in a voxel at readout time t , for a Lorentzian distribution of spins is [12]:

$$S_{\text{Lorentzian}} = \left| \rho e^{-(\tau+t)R_2 - |(\tau-t)|R_2'} \right|, \quad (1)$$

where τ denotes the period between excitation and refocusing ($\tau = \text{TE}_{\text{SE}}/2$), t denotes the time following refocusing (such that the spin echo forms at $t = \tau$), ρ is the pseudo proton density, including the proton density and appropriate T1-weighting factors influencing longitudinal magnetization prior to excitation, R_2 and R_2' denote transverse relaxation rates associated with irreversible and reversible processes, respectively. The full width at half-maximum (FWHM) of the corresponding Lorentzian distribution is $2R_2'$. Complete spoiling of transverse magnetization before each excitation, and the same R_2 across all frequency components (as may be expected for most tissues that contain only water, and where fat does not exist or has been suppressed) is assumed.

The key difference between left- and right-hand sides of the SE in a GESSE sequence is reflected in Eq. (1) by the exponential term for R_2' : the argument has an absolute value, indicating that $R_2 - R_2'$ governs signal evolution (which could be decay or growth) on the left-hand side (irreversible processes dephase spins and reversible processes

rephase spins), while $R_2 + R_2'$ governs signal evolution (decay) before the refocusing pulse and on the right-hand side (both irreversible and reversible transverse relaxation dephase spins).

For a Gaussian distribution of spins [12]:

$$S_{\text{Gaussian}} = \left| \rho e^{-(\tau+t)R_2 - ((\tau-t)\sigma)^2/2} \right|, \quad (2)$$

where the FWHM is $2\sqrt{2\log(2)}\sigma$. All other quantities are the same as those for the Lorentzian distribution, except the reversible transverse relaxation term is now σ rather than R_2' .

For a Voigt distribution of spins [32, 33]:

$$S_{\text{Voigt}} = \left| \rho e^{-(\tau+t)R_2 - |(\tau-t)|R_2' - ((\tau-t)\sigma)^2/2} \right|, \quad (3)$$

such that the Voigt distribution becomes equivalent to the Lorentzian distribution when $\sigma = 0$ and to the Gaussian distribution when $R_2' = 0$, and where the FWHM $\approx R_2' + \sqrt{(R_2')^2 + 8\log(2)\sigma^2}$ [32].

For a SAS distribution of spins [10]:

$$S_{\text{SAS}} = \left| \rho e^{-(\tau+t)R_2 - 2^{(1-\alpha)}|(\tau-t)|^\alpha} \right|, \quad (4)$$

where σ describes the width of the distribution and α describes the shape of the distribution with $1 \leq \alpha \leq 2$, such that the SAS distribution becomes equivalent to the Lorentz distribution when $\alpha = 1$ and to the Gaussian distribution when $\alpha = 2$. When α is not 1 or 2, the underlying distribution has no analytic form [10].

Subjects

Six consecutive patients (ages 60 ± 18 years, weight 64 ± 19 kg) diagnosed with cervical squamous cell carcinoma (International Federation of Gynecology, FIGO, stage IIB-IIIB [34], were imaged in this Institutional Review Board-approved study following their written informed consent. Biological phantoms (one potato and one lemon) were used to assess potential effects of differences in microscopic structure on transverse relaxation: potato was used due to its relatively homogeneous isotropic texture (no strongly ordered anisotropic structures such as fibers or canals), and lemon was used due to its relatively anisotropic fibrous texture (with fibers oriented in multiple directions which might potentially mirror muscle fibers of various orientations in the cervix).

Data acquisition

Data were acquired at 3 T (Verio, IMRIS, Minnetonka, MN). Matrix coils, specifically the 6-element body and 24-element spine (only the subset near the pelvis)

were used. Two-dimensional T_2 -weighted turbo-spin-echo (TSE) images were acquired in axial, coronal, and sagittal orientations, using the parameters: repetition time (TR) = 7740 ms, echo time (TE) = 102 ms, flip angle = 140° , field of view (FOV) = $22 \times 22 \text{ cm}^2$, matrix = 256×320 , resolution = $0.9 \times 0.7 \text{ mm}^2$, 2 averages, 30 slices with a thickness of 4 mm and gap of 0.8 mm. Two-dimensional axial, GESSE images were acquired on patients with TR = 2.5 s, TE = 80 ms, gradient-echo spacing was $\Delta\text{TE} = 4.52 \text{ ms}$, and the TE values were: 48.36, 52.88, 57.4, 61.92, 66.44, 70.96, 75.48, 80, 84.52, 89.04, 93.56, 98.08, 102.6, 107.12 and 111.64 ms, such that 8th of 15 unipolar gradient echoes coincided with the spin echo. FOV was $38 \times 38 \text{ cm}^2$, matrix = 128×128 , resolution = $2.969 \times 2.969 \text{ mm}^2$, 19 slices were acquired with a thickness of 4 mm, gap of 2 mm, and 1 average. The SE was at the center of the train of gradient echoes, such that readouts were symmetrical with respect to the SE. All GESSE parameters were the same for biological phantoms except for the acquisition of more echoes and fewer slices: the 16th of 31 unipolar gradient echoes coincided with the spin echo, and gradient-echo spacing was smaller at $\Delta\text{TE} = 2.48 \text{ ms}$, and the TE values were: 42.80, 45.28, 47.76, 50.24, 52.72, 55.2, 57.68, 60.16, 62.64, 65.12, 67.6, 70.08, 72.56, 75.04, 77.52, 80, 82.48, 84.96, 87.44, 89.92, 92.4, 94.88, 97.36, 99.84, 102.32, 104.8, 107.28, 109.76, 112.24, 114.72 and 117.2 ms, for 12 slices. Frequency-encoding was superior (S) to inferior (I), and phase encoding was anterior (A) to posterior (P). Higher cellularity in malignancy is thought to restrict motion of water molecules resulting in lower apparent diffusion coefficients (ADC). On patients, two-dimensional axial, diffusion-weighted images (DWI) were also acquired, and ADCs were calculated for tumor localization from readout segmented multi-shot EPI at $b = 0$ and $600 \text{ mm}^2/\text{s}$, fat saturation, TE = 56 ms, TR = 5.7 s, FOV = $35 \times 28 \text{ cm}^2$, matrix = 160×128 , resolution = $2.1875 \times 2.1875 \text{ mm}^2$, 34 slices with a thickness of 4.8 mm, gap of 0 mm, and three averages. Macroscopic magnetic field inhomogeneities were minimized by shimming in a sub-volume covering the phantom, or the tumor and surrounding tissues, in all cases.

Models and fitting

Matlab was used to fit GESSE signals to all models (R2017b, Mathworks, Natick, MA). Before model fitting, magnitude data was corrected for bias (from a positive noise floor), as described in [35]:

$$N_{\text{SDcorr}} = \text{std}(R_{\text{uncorr}}) / \sqrt{2 - \pi/2}, \quad (5)$$

$$S_{\text{corr}} = \sqrt{\left| \text{mean}(S_{\text{uncorr}})^2 - N_{\text{SDcorr}}^2 \right|}, \quad (6)$$

where a region-of-interest (ROI) in the background is manually drawn to determine R_{uncorr} , the level of uncorrected noise, N_{SDcorr} denotes the corrected noise standard deviation, S_{uncorr} the uncorrected signal, and S_{corr} the corrected signal. Voxels with SNR higher than three for at least more than the “number of maximum fitting parameters” (i.e., $\text{SNR} > 3$ at a minimum of 5 TEs) number of echo times were analyzed further. For each voxel, data averaging to further reduce noise was performed over a neighborhood of 3×3 pixels, in-plane. For all models, the *lsqnonlin* function was used to perform fitting. For all four models, ρ and R_2 , additionally, for the Lorentzian model, R_2' ; for the Gaussian model, σ ; for the Voigt model, R_2' and σ ; and finally for the SAS model, σ and α were obtained from fits of S vs TE. Constraints were that $\rho \geq 0$, $R_2 \geq 0$, $R_2' \geq 0$, $\sigma \geq 0$ and $1 \leq \alpha \leq 2$. For subsequent model comparison, sums of the squared residual errors (SSEs) between the data and each fit were also calculated.

Model comparison

In modeling, smaller SSEs can generally be achieved by increasing the number of parameters, however, parameter variance may be high when more parameters result in overfitting. Akaike's Information Criterion (AIC) is based on information theory and for problems involving model selection, it offers an objective solution: AIC assesses models based on how much information they can retain, weighing improvements in SSEs by the additional number of parameters used to achieve these improvements. When the number of parameters in a model is on the order of the number of available measurements, Akaike's information criterion is corrected using a (second-order) small-sample bias adjustment [36].

The corrected Akaike's information criterion, AICc, was used for model comparison. AICc was calculated for each model as described in [37]:

$$\text{AICc} = \frac{\text{SSE}}{N_{\text{SDcorr}}} + 2p + \frac{2p(p+1)}{(n-p-1)}, \quad (7)$$

where N_{SDcorr} is the standard deviation of noise, p denotes the number of model parameters, and n denotes the number of available data points. In our case, $p = 3$ for Lorentzian and Gaussian models, $p = 4$ for Voigt and SAS models, and $n = 15$. The model with higher estimated information content has lower AICc values and is considered the better model.

AICc differences relative to the model with the minimum AICc were calculated for all models. The likelihood of each model was estimated based on AICc differences and Akaike weights were calculated for each model as follows:

$$\text{AICc}_{\text{difference}}(m) = \text{AICc}(m) - \text{AICc}_{\text{minimum}}, \quad (8)$$

$$\text{AICc}_{\text{likelihood}}(m) = e^{-\text{AICc}_{\text{difference}}(m)/2}, \quad (9)$$

$$\text{AICc}_{\text{weight}}(m) = \frac{\text{AICc}_{\text{likelihood}}(m)}{\sum_{i=1}^4 \text{AICc}_{\text{likelihood}}(i)}, \quad (10)$$

for each model, $m = 1$ (Lorentzian), 2 (Gaussian), 3 (Voigt), 4 (SAS). The best performing model has the minimum AICc value, an AICc difference of 0, likelihood of 1, and weight of 1. AICc maps were generated, indicating the model with the minimum AICc, at each voxel.

Field inhomogeneity effects

We estimated levels of background macroscopic field inhomogeneity from GESSE acquisitions by saving both magnitude and phase data. The phase accumulation between the first two gradient echoes was determined and unwrapped using the Statistical Parametric Mapping software package SPM12, and function pm_unwrap [33] (www.fil.ion.ucl.ac.uk/spm). Field maps (mT) were calculated by dividing the unwrapped phase difference by the TE difference:

$$B_0 \text{ Fieldmap} = \frac{\text{pm_unwrap}\left(|S_2|e^{i\angle(S_2)}/e^{i\angle(S_1)}\right)}{2\pi\gamma(\text{TE}_2 - \text{TE}_1)}, \quad (11)$$

where S_1 denotes the complex signal at TE_1 and S_2 denotes the complex signal at TE_2 . Phase unwrapping failed in areas of low signal where there was extensive phase accumulation. Such voxels (typically seen in the rectum due to air, or at the edges of the bladder due to motion) were excluded from further analysis since their field distributions were unknown. Field gradient magnitudes along in-plane and through-plane directions (G_x , G_y , and G_z , mT/m) and their root mean square

(RMS) were estimated from central differences of the B_0 fieldmap as follows:

$$G_i = \frac{|\text{Fieldmap}_{\text{Next voxel along } i} - \text{Fieldmap}_{\text{Previous voxel along } i}|}{2 \times (\text{Inter voxel distance along } i)} \text{ for } i = x, y, z, \quad (12)$$

$$G_{\text{RMS}} = \sqrt{G_x^2 + G_y^2 + G_z^2}. \quad (13)$$

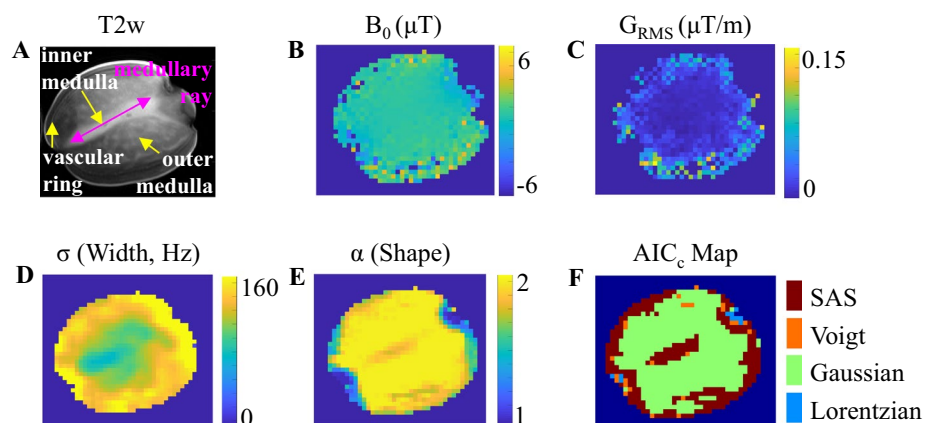
Results

Field distribution in biological phantom: potato (isotropic)

Magnetic field distribution could be reliably assessed in most areas of the potato. Figure 2 shows a mid-tuber transverse slice with the maximum extension of the potato along the R-L direction. The inner and outer medulla, medullary ray and vascular ring are clearly visible and labeled on the T_2 -weighted image (Fig. 2a). The B_0 field map (Fig. 2b) and G_z field map (Fig. 2c) were quite uniform, remaining well under 0.02 mT and 0.002 mT/mm in the center, with slightly higher values around the periphery. The width parameter σ nearly doubled near the periphery relative to the center (Fig. 2d). The shape parameter α indicated a nearly Gaussian field distribution with values close to 2 in most of the outer medulla, with lower values of 1.5–1.8 only near the center of the inner medulla, and around the vascular ring (Fig. 2e).

In terms of information content, the Gaussian distribution sufficiently represented most of the outer medulla (Fig. 2f, green), and the SAS distribution performed better only near the center of the inner medulla and around the vascular ring (Fig. 2f, maroon). Lorentzian or Voigt distributions were not representative of signal decay except for a few voxels at the stem and bud ends of the tuber (Fig. 2f, blue and

Fig. 2 Sample potato mid-tuber transverse slice. **A** T_2 weighted TSE image (arbitrary units, au.). **B** B_0 field map (μT). **C** G_{RMS} field gradient map ($\mu\text{T/m}$). **D** σ , SAS width parameter (Hz). **E** α , SAS shape parameter (no unit). **F** Best performing distribution according to AICc (no unit)



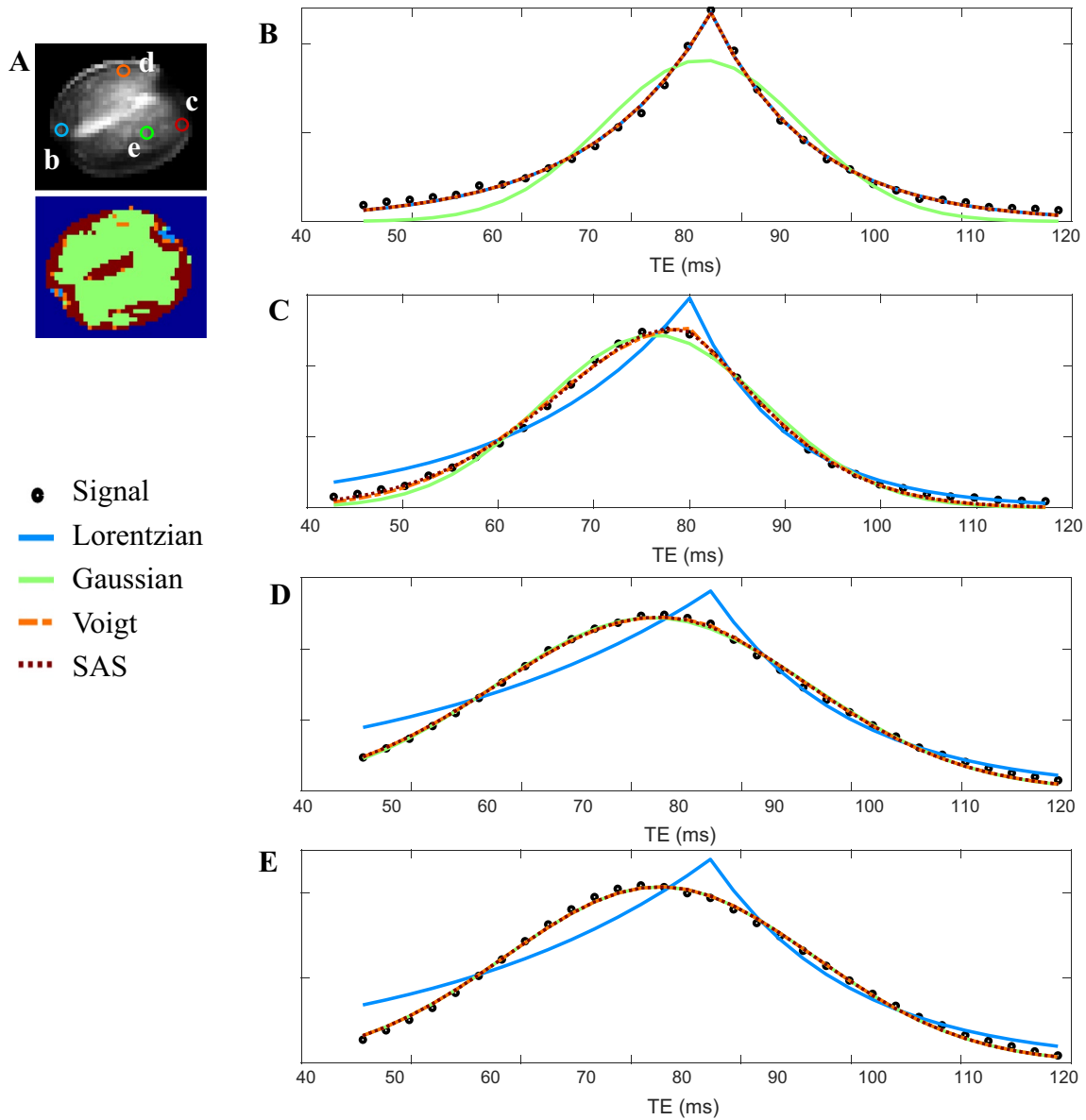


Fig. 3 Sample potato GESSE signal (au.) and best fits to each distribution. **A** Four sample voxels are shown on a GESSE image (averaged over all TEs). **B** Lorentzian distribution performed best ($\alpha=1$).

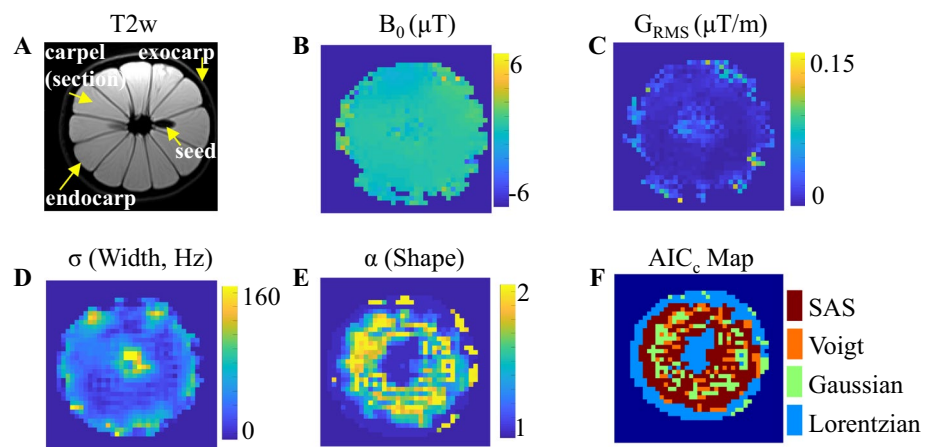
orange, respectively). Sample GESSE signal and best fits to each distribution are shown in Fig. 3b–e, for four voxel positions depicted in Fig. 3a. Voxel b (Fig. 3b) and voxel e (Fig. 3e) show purely Lorentzian and purely Gaussian distributions, respectively, while voxels c and d (Fig. 3c and d) are intermediate scenarios where Voigt and SAS distributions improved fits.

C SAS distribution performed best ($\alpha=1.61$). **D** Voigt distribution performed best ($\alpha=1.92$). **E** Gaussian distribution performed best ($\alpha=2$)

Field distribution in biological phantom: lemon (tubular)

Magnetic field distribution could also be reliably assessed in most areas of the lemon, excluding the exocarp (peel) and seeds. Figure 4 shows a mid-berry transverse slice. The exocarp and endocarp, the individual sections (carpels) and

Fig. 4 Sample lemon mid-berry transverse slice. **A** T_2 weighted TSE image (au.). **B** B_0 field map (μT). **C** G_{RMS} field gradient map ($\mu\text{T}/\text{m}$). **D** σ , SAS width parameter (Hz). **E** α , SAS shape parameter. **F** Best performing distribution according to AICc



location of some seeds are visible and labeled on the T_2 -weighted image (Fig. 4a). The B_0 and G_z field maps (Fig. 4b and c, respectively) are also quite uniform for the lemon, with slightly higher G_z values only seen near the exocarp and seeds. The width parameter σ increases in a few areas near the exocarp and seeds but remains low throughout most of the endocarp (Fig. 4d). The shape parameter α indicates a nearly Lorentzian field distribution with values close to 1 only near the exocarp and seeds, with higher values of 1.3–2 observed throughout the endocarp (Fig. 4e).

In terms of information content, the Lorentzian distribution performed best only near the exocarp and seeds (Fig. 4f, blue), and the SAS distribution performed best at the peripheral and central edges of the endocarp (Fig. 4f, maroon). Gaussian and Voigt distributions performed best throughout most of the central endocarp (Fig. 4f, green and orange, respectively). Sample GESSE signal and best fits to each distribution are shown in Fig. 5b–e, for four voxel positions depicted in Fig. 5a. Voxel b (Fig. 5b) and voxel e (Fig. 5e) show signals best represented by Lorentzian and Gaussian distributions, respectively, while voxels c and d (Fig. 5c and d) show intermediate scenarios where Voigt and SAS distributions performed best.

Field distribution in human pelvis, cervix, and cancer

Figure 6 presents data from Patient X, with Stage IIIB cervical squamous cell carcinoma, over three consecutive transverse slices. The MRI report indicates a nearly circumferential mass within the cervix, showing restricted diffusion, invading through the cervical stroma into parametrial tissues on the right, with A/P, S/I, and Right/Left (R/L) dimensions up to 3.6 cm \times 3.3 cm \times 4.5 cm, respectively, and no

involvement of the bladder or rectum. T_2 -weighted images are shown, with R/L and A/P coordinates labeled (Fig. 6a). ADC maps are shown, and the bladder, cervix (tumor and normal), and rectum are labeled in Fig. 6b. The remaining parts of Figs. 6 and 7 are magnified displays (as indicated by the yellow rectangle, Fig. 6c). Pink and red ROIs are provided to help visualization of field maps and fitting parameters, where reference structures are not clearly visible. B_0 and G_z field maps were calculated everywhere except where phase-unwrapping was not possible (mostly within the rectum, periphery of the bladder etc.), and were also quite uniform for the patient (Fig. 6d and e, respectively). Fitting results for the same patient are presented in Fig. 7. The width parameter σ was within the 120–160 Hz range in the PL quadrant, the 0–30 Hz range in small areas in the mid-R and AL, and the 80–90 Hz range in the remainder of the ROI (Fig. 7a). The shape parameter α indicates an intermediate field distribution in the PL quadrant and mid-A to RA, a nearly Gaussian distribution is found in the mid-R to PR and AL, and a nearly Lorentzian distribution in two small regions closer to the center of the ROI (Fig. 7b).

In terms of information content, the SAS distribution was representative of most of the ROI in the PL quadrant and mid-A to RA (Fig. 7c, maroon, near where the shape parameter indicated an intermediate distribution). The Lorentzian distribution performed best near areas where the shape parameter also indicated a Lorentzian distribution (Fig. 7c, blue). The Gaussian distribution performed best near areas where the shape parameter also indicated a Gaussian distribution (Fig. 7c, green). The Voigt distribution performed best in fewer voxels compared to the other distributions (Fig. 7c, orange, also near where the shape parameter indicated an intermediate distribution). Sample best fits to each distribution are shown in Fig. 8b–e, for four

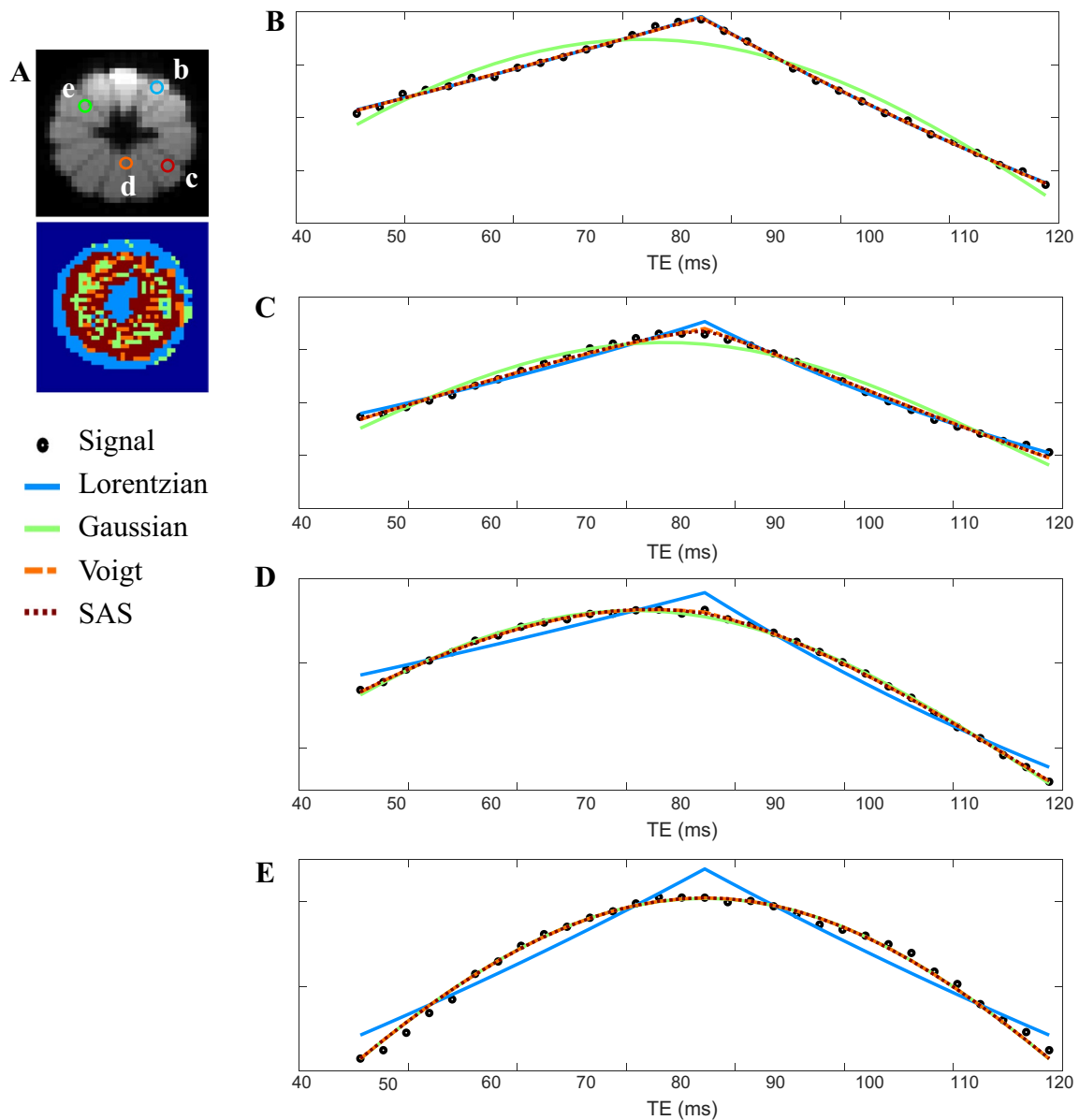


Fig. 5 Sample lemon GESSE signal (au.) and best fits to each distribution. **A** Four sample voxels are shown on a GESSE image (averaged over all TEs). **B** Lorentzian distribution performed best

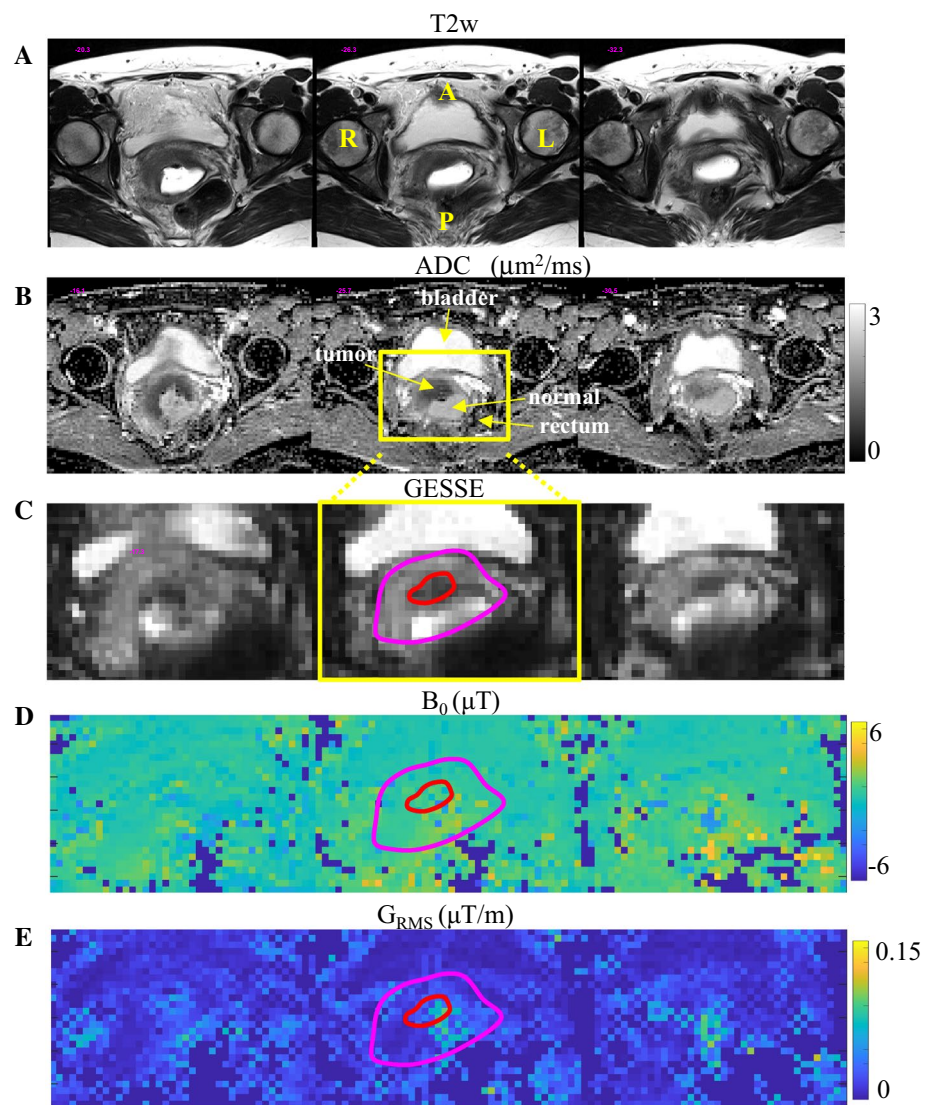
($\alpha=1.02$). **C** SAS distribution performed best ($\alpha=1.29$). **D** Voigt distribution performed best ($\alpha=1.80$). **E** Gaussian distribution performed best ($\alpha=1.98$)

voxel positions depicted in Fig. 8a. Voxel b (Fig. 8b) and voxel e (Fig. 8e) show signals best represented by Lorentzian and Gaussian distributions, respectively, while voxels c and d (Fig. 8c and d) show intermediate scenarios where Voigt and SAS distributions were the most representative distributions, respectively.

Figure 9 presents data from Patient Y, with Stage IIB cervical squamous cell carcinoma, on a single transverse

slice. The MRI report indicates a cervical mass measuring approximately $4.4 \text{ cm} \times 6.6 \text{ cm} \times 6 \text{ cm}$ (A/P, S/I, and R/L, respectively), involving the entire endocervical canal, lower uterine segment, and superior half of the vagina, with almost certain involvement of adjacent parametrial tissues, and possible involvement of the posterior bladder wall and anterior rectal walls. The T_2 -weighted image and ADC map are shown in Fig. 9a and b, respectively.

Fig. 6 Sample data from Patient X with Stage IIIB cervical squamous cell carcinoma. **A** T_2 weighted TSE images (au.). **B** Apparent Diffusion Coefficient, ADC, images ($\mu\text{m}^2/\text{ms}$). **C** GESSE images (averaged over all TEs, au.). **D** B_0 Field maps (μT). **E** G_{RMS} Field gradient maps ($\mu\text{T}/\text{m}$), in three adjacent slices

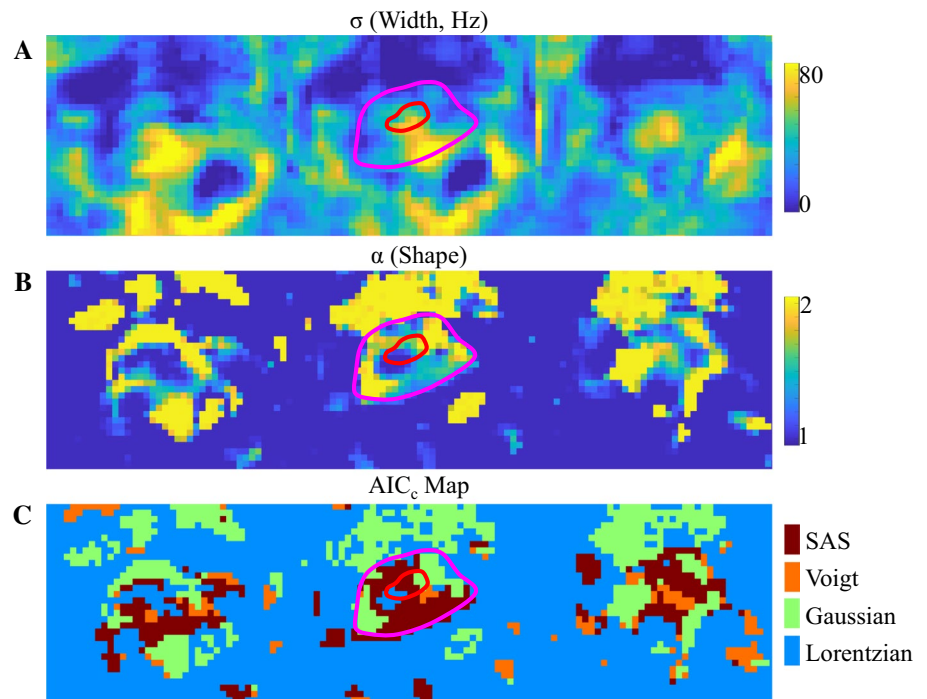


The rest of Fig. 9 is magnified (as indicated by the yellow rectangle), along with ROIs (in pink) to help visualization of field maps and fitting parameters (where reference structures may not be clearly visible). B_0 and G_z field maps were also very uniform for this patient (Fig. 9c and d, respectively). The width parameter σ was within 0–60 Hz across most of the ROI, with few values approaching 80 Hz near the center of the ROI (Fig. 9e and f, show comparable results without and with averaging for noise reduction, respectively). The shape parameter α indicates a nearly Gaussian field distribution on the R and PL, and a nearly Lorentzian distribution almost everywhere else,

with very few voxels near the center of the ROI indicating intermediate distributions (Fig. 9g).

In terms of information content, the Lorentzian and Gaussian distributions were representative of nearly all the relevant anatomy (Fig. 9h, blue and green, respectively, also in agreement with the shape parameter). The SAS and Voigt distributions performed best in very few voxels near the center (Fig. 9h, maroon and orange, respectively). Sample best fits to each distribution are shown in Fig. 10b–e, for four voxel positions depicted in Fig. 10a. Voxel b (Fig. 10b) and voxel e (Fig. 10e) show signals best represented by Lorentzian and Gaussian

Fig. 7 Patient X. **A** σ , SAS width parameter (Hz). **B** α , SAS shape parameter, **C** Best performing distribution according to AICc



distributions, respectively, while voxels c and d (Fig. 10c and d) show intermediate scenarios where SAS and Voigt distributions were the most representative distributions, respectively.

Muscle data is also provided in Figs. 8f and 10f. In both cases, $R_2 > R_2'$ and the left side of the SE, where rephasing by reversible processes works against dephasing by irreversible processes, decays.

Discussion and conclusions

At 3 T, in much of the female pelvis, transverse relaxation as measured by GESSE, did not generally follow a simple mono-exponential decay corresponding to a Lorentzian intra-voxel frequency distribution, and non-Lorentzian distributions performed substantially better. Clear and systematic deviations from mono-exponential decays were observed in both biological phantoms and the human cervix. The potato in this study, oriented with its medullary ray orthogonal to the main magnetic field B_0 , had larger width parameters σ (Fig. 2) compared to prior results on one oriented parallel to B_0 , in agreement with observations on a pineapple [10] and might also suggest some anisotropy in the potato. The lemon produced noisier maps and its T_2 was much longer (over 200 ms)

compared to potato (~ 30 – 50 ms) and biological tissue T_2 values [38], which might potentially underlie reduced fitting performance related to limited irreversible relaxation (when imaging parameters relevant to the cervix are used). Our findings not only have theoretical support [4, 5, 9], but also agree well with previous observations in the brain, lungs, prostate, teeth, and blood, using either multi-echo GE or GESSE imaging [10–12, 39].

Deviations from mono-exponential decay have been suggested to potentially result from the interaction between macroscopic gradients (which, especially at higher field strengths, can lead to higher susceptibility effects from interfaces between air and tissue, or bone and tissue) and non-ideal slice profiles [40] (which can deviate from the assumed rectangular profiles and appear more Gaussian in reality [41]). Calculated field maps and field gradients show that the background fields are quite uniform. Additionally, while some larger width parameters coincide with larger shape parameters (closer to 2, indicating a more Gaussian distribution), in many cases smaller width parameters, and smaller gradient G_{RMS} values often also coincide with larger shape parameters, with no apparent overlap. While this mechanism could indeed contribute, it fails to completely explain the observed deviation from mono-exponential decays. The apparent lack of correlation between shape and width parameters and the lack

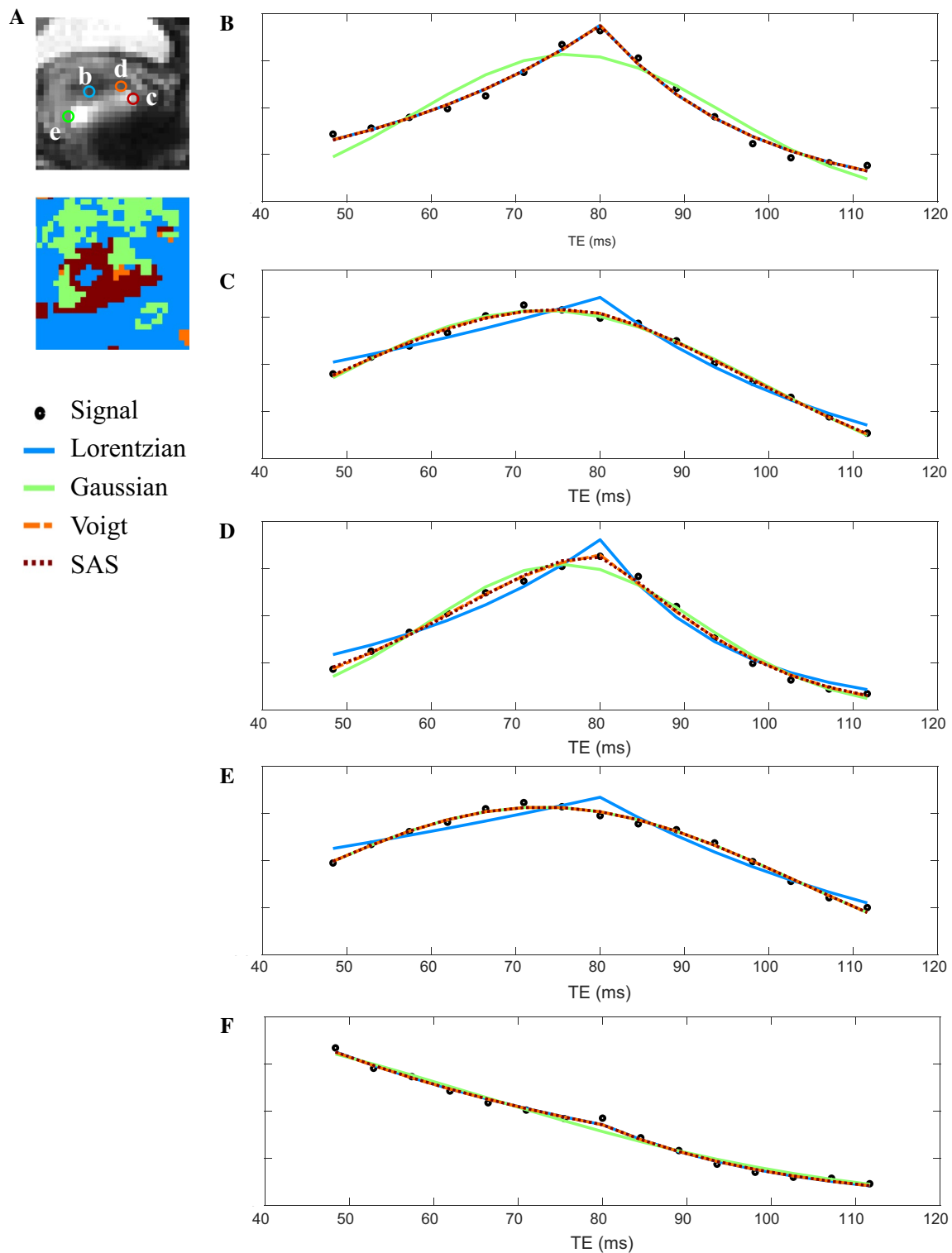


Fig. 8 Patient X, sample GESSE signal (au.) and best fits to each distribution. **A** Four sample voxels are shown on a GESSE image (averaged over all TEs). **B** Lorentzian distribution performed best ($\alpha=1.01$). **C** SAS distribution performed best ($\alpha=1.76$). **D** Voigt

distribution performed best ($\alpha=1.49$). **E** Gaussian distribution performed best ($\alpha=2$). **F** Muscle ($R_2=33\text{ ms} > R_2'=12\text{ ms}$, note corresponding decay on the left side of the SE)

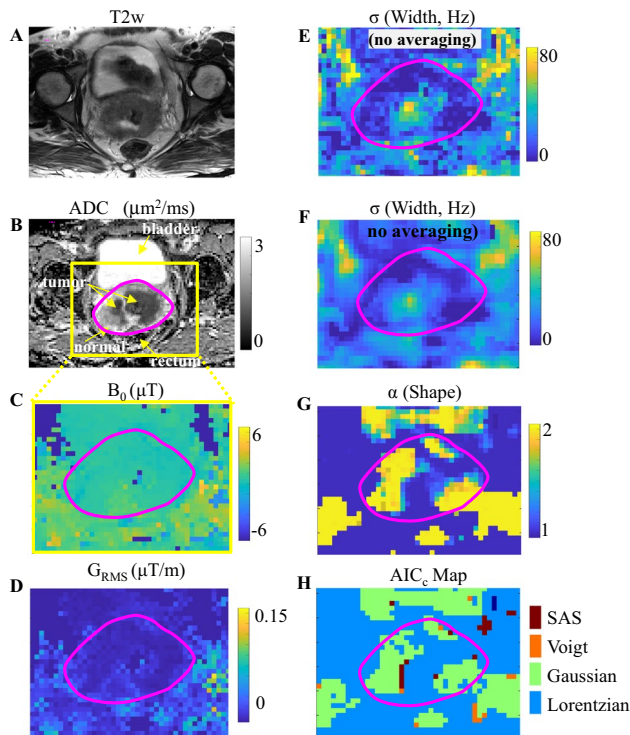


Fig. 9 Sample data from Patient Y with Stage IIB cervical squamous cell carcinoma. **A** T_2 weighted TSE images (au.). **B** Apparent Diffusion Coefficient, ADC, images ($\mu\text{m}^2/\text{ms}$). **C** B_0 Field maps (μT). **D** G_{RMS} Field gradient maps ($\mu\text{T}/\text{m}$). **E** GESSE images (averaged over all TEs, au.). **F** σ , SAS width parameter (Hz). **G** α , SAS shape parameter. **H** Best performing distribution according to AICc

of influence of averaging on background gradient effects, provide further support that our observations might indeed be reflections of underlying biological circumstances.

Voigt and SAS distributions have one additional parameter compared to Lorentzian and Gaussian distributions. When the shape parameter α was near 1 or 2, additional parameters were not justified, and the best performing distributions were Lorentzian and Gaussian, respectively. When the shape parameter had intermediate values, the additional parameters of Voigt and SAS distributions were justified, and the best performing distributions were the Voigt and SAS as expected. However, the Voigt distribution was needed much less frequently than the SAS distribution overall. Even in cases when an

extra parameter was justified and the Voigt distribution performed best in terms of information content, the difference between the best performing Voigt and next-best performing SAS distributions were miniscule, especially in the human cases. The central peak of a Lorentzian distribution is narrower than the central peak of a Gaussian distribution, for similar reversible transverse relaxation terms R_2' and σ (Fig. 1, inset A), while the tail of a Lorentzian distribution includes a wider range of frequencies than the tail of a Gaussian distribution (Fig. 1, inset B), as expected from the differences in their FWHMs. Since both two-parameter distributions SAS and Voigt can represent Lorentzian and Gaussian distributions as well as intermediate cases, they might be expected to perform more similarly, however, the ability to place upper and lower bounds on one of the SAS parameters ($1 \leq \alpha \leq 2$, while $R_2 \geq 0$, $R_2' \geq 0$, $\sigma \geq 0$) may potentially have rendered fitting to the SAS model less sensitive to initial values and local minima. Given the same assumptions underlying validity of SAS and Voigt distributions (i.e., no considerable fat content or efficient fat suppression in order to maintain symmetry [10]), a separate Voigt implementation may not be necessary.

Improved modeling, beyond Lorentzian fitting, is needed in the female pelvis; Gaussian, Voigt, and SAS models minimize information loss, and could improve the accuracy of parameter estimation. However, our study is limited to a small number of cases. To determine the degree to which these more accurately characterized MR parameters will correlate with biomarkers of interest, i.e., hypoxia or improve clinically important quantitative assessments requires further studies, including more cases, and ideally, using a gold standard for hypoxia (e.g., immunohistochemistry, pO_2 microelectrodes, and/or PET and ROC analysis).

In conclusion, modeling irreversible transverse relaxation with Gaussian and intermediate (SAS and Voigt) distributions, as opposed to a Lorentzian distribution, improves characterization of GESSE signals in cervical cancers at 3 T; existence of through plane gradients may contribute to deviations from Lorentzian but are not the only reason for the observed deviations. Improved characterization of underlying signals leads to more accurate determination of fit parameters, increasing the potential for identifying biomarkers of relevant physiological variables.

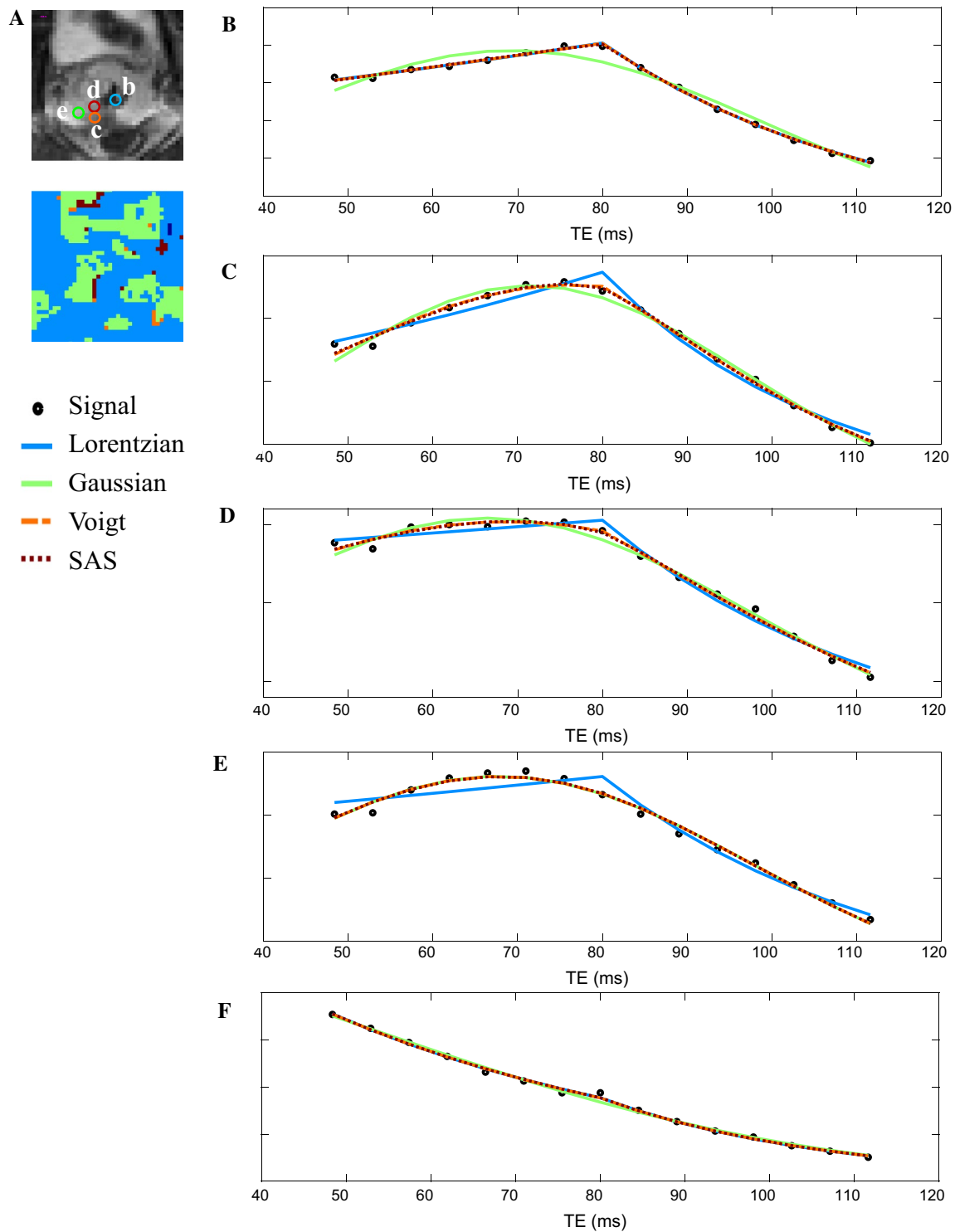


Fig. 10 Patient Y, sample GESSE signal (au.) and best fits to each distribution. **A** Four sample voxels are shown on a GESSE image (averaged over all TEs). **B** Lorentzian distribution performed best ($\alpha=1.04$). **C** SAS distribution performed best ($\alpha=1.51$). **D** Voigt

distribution performed best ($\alpha=1.52$). **E** Gaussian distribution performed best ($\alpha=1.95$). **F** Muscle ($R_2=30$ ms $>$ $R_2'=8$ ms, note corresponding decay on the left side of the SE)

Acknowledgements The authors would like to thank Prof. Robert Mulkern and Dr. Mukund Balasubramanian for the GESSE pulse sequence and suggestions, and Dr. Akila Viswanathan for clinical guidance.

Funding The authors did not receive support from any organization for the submitted work.

Declarations

Conflict of interest The authors have no relevant financial or non-financial interests to disclose.

Ethical approval Ethics approval was obtained from the ethics committee of Brigham and Women's Hospital, Boston, MA. The procedures used in this study adhere to the tenets of the Declaration of Helsinki.

Informed consent Informed consent was obtained from all participants included in the study.

References

- Schenck JF (1996) The role of magnetic susceptibility in magnetic resonance imaging: MRI magnetic compatibility of the first and second kinds. *Med Phys* 23(6):815–850
- Hopkins JA, Wehrli FW (1997) Magnetic susceptibility measurement of insoluble solids by NMR: magnetic susceptibility of bone. *Magn Reson Med* 37(4):494–500
- Yablonskiy DA (1998) Quantitation of intrinsic magnetic susceptibility-related effects in a tissue. *Magn Reson Med* 39:417–428
- Yablonskiy DA, Haacke EM (1994) Theory of NMR signal behavior in magnetically inhomogeneous tissues: the static dephasing regime. *Magn Reson Med* 32:749–763
- Kiselev VG, Novikov DS (2018) Transverse NMR relaxation in biological tissues. *Neuroimage* 182:149–168
- Kiselev VG, Strecker R, Ziyeh S, Speck O, Hennig J (2005) Vessel size imaging in humans. *Magn Reson Med* 53(3):553–563
- Ma J, Wehrli FW (1996) Method for image-based measurement of the reversible and irreversible contribution to the transverse-relaxation rate. *J Magn Reson B* 111(1):61–69
- Yablonskiy DA, Haacke EM (1997) An MRI method for measuring T2 in the presence of static and RF magnetic field inhomogeneities. *Magn Reson Med* 37(6):872–876
- Slotboom J, Boesch C, Kreis R (1998) Versatile frequency domain fitting using time domain models and prior knowledge. *Magn Reson Med* 39(6):899–911
- Steidle G, Schick F (2021) A new concept for improved quantitative analysis of reversible transverse relaxation in tissues with variable microscopic field distribution. *Magn Reson Med* 85(3):1493–1506
- Balasubramanian M, Polimeni JR, Mulkern RV (2019) In vivo measurements of irreversible and reversible transverse relaxation rates in human basal ganglia at 7 T: making inferences about the microscopic and mesoscopic structure of iron and calcification deposits. *NMR Biomed* 32(11):e4140
- Mulkern RV, Balasubramanian M, Mitsouras D (2015) On the Lorentzian versus Gaussian character of time-domain spin-echo signals from the brain as sampled by means of gradient-echoes: implications for quantitative transverse relaxation studies. *Magn Reson Med* 74(1):51–62
- Zapp J, Domsch S, Weingärtner S, Schad LR (2017) Gaussian signal relaxation around spin echoes: Implications for precise reversible transverse relaxation quantification of pulmonary tissue at 1.5 and 3 Tesla. *Magn Reson Med* 77(5):1938–1945
- Ciris PA, Balasubramanian M, Seethamraju RT, Tokuda J, Scalera J, Penzkofer T, Fennessy FM, Tempany-Afdhal CM, Tuncali K, Mulkern RV (2016) Characterization of gradient echo signal decays in healthy and cancerous prostate at 3T improves with a Gaussian augmentation of the mono-exponential (GAME) model. *NMR Biomed* 29(7):999–1009
- Dou W, Mastrogiacomo S, Veltien A, Alghamdi HS, Walboomers XF, Heerschap A (2018) Visualization of calcium phosphate cement in teeth by zero echo time (1) H MRI at high field. *NMR Biomed* 31(2):e3859
- Spees WM, Yablonskiy DA, Oswood MC, Ackerman JJ (2001) Water proton MR properties of human blood at 1.5 Tesla: magnetic susceptibility, T(1), T(2), T*(2), and non-Lorentzian signal behavior. *Magn Reson Med* 45(4):533–542
- Marshall I, Higinbotham J, Bruce S, Freise A (1997) Use of Voigt lineshape for quantification of in vivo 1H spectra. *Magn Reson Med* 37(5):651–657
- Zhang L, Zhao Y, Chen Y, Bie C, Liang Y, He X, Song X (2019) Voxel-wise Optimization of Pseudo Voigt Profile (VOPVP) for Z-spectra fitting in chemical exchange saturation transfer (CEST) MRI. *Quant Imaging Med Surg* 9(10):1714–1730
- Lim K, Chan P, Dinniwel R, Fyles A, Haider M, Cho YB, Jaffray D, Manchul L, Levin W, Hill RP, Milosevic M (2008) Cervical cancer regression measured using weekly magnetic resonance imaging during fractionated radiotherapy: radiobiologic modeling and correlation with tumor hypoxia. *Int J Radiat Oncol Biol Phys* 70(1):126–133
- Grigsby PW, Malyapa RS, Higashikubo R, Schwarz JK, Welch MJ, Huettner PC, Dehdashti F (2007) Comparison of molecular markers of hypoxia and imaging with (60)Cu-ATSM in cancer of the uterine cervix. *Mol Imaging Biol* 9(5):278–283
- Fyles A, Milosevic M, Pintilie M, Syed A, Levin W, Manchul L, Hill RP (2006) Long-term performance of interstitial fluid pressure and hypoxia as prognostic factors in cervix cancer. *Radiother Oncol* 80(2):132–137
- Fyles A, Milosevic M, Hedley D, Pintilie M, Levin W, Manchul L, Hill RP (2002) Tumor hypoxia has independent predictor impact only in patients with node-negative cervix cancer. *J Clin Oncol* 20(3):680–687
- Lancaster JA, Carrington BM, Sykes JR, Jones AP, Todd SM, Cooper R, Buckley DL, Davidson SE, Logue JP, Hunter RD, West CM (2002) Prediction of radiotherapy outcome using dynamic contrast enhanced MRI of carcinoma of the cervix. *Int J Radiat Oncol Biol Phys* 54(3):759–767
- Lyng H, Sundfor K, Rofstad EK (2000) Changes in tumor oxygen tension during radiotherapy of uterine cervical cancer: relationships to changes in vascular density, cell density, and frequency of mitosis and apoptosis. *Int J Radiat Oncol Biol Phys* 46(4):935–946
- Hockel M, Knoop C, Schlenger K, Vorndran B, Bausmann E, Mitze M, Knapstein PG, Vaupel P (1993) Intratumoral pO2 predicts survival in advanced cancer of the uterine cervix. *Radiother Oncol* 26(1):45–50
- Lyng H, Sundfor K, Trope C, Rofstad EK (2000) Disease control of uterine cervical cancer: relationships to tumor oxygen tension, vascular density, cell density, and frequency of mitosis and apoptosis measured before treatment and during radiotherapy. *Clin Cancer Res* 6(3):1104–1112
- Charra-Brunaud C, Harter V, Delannes M, Haie-Meder C, Quetin P, Kerr C, Castelain B, Thomas L, Peiffert D (2012) Impact of 3D image-based PDR brachytherapy on outcome of patients treated for cervix carcinoma in France: results of the French STIC prospective study. *Radiother Oncol* 103(3):305–313

28. Hoskin PJ, Carnell DM, Taylor NJ, Smith RE, Stirling JJ, Daley FM, Saunders MI, Bentzen SM, Collins DJ, d'Arcy JA, Padhani AP (2007) Hypoxia in prostate cancer: correlation of BOLD-MRI with pimonidazole immunohistochemistry-initial observations. *Int J Radiat Oncol Biol Phys* 68(4):1065–1071
29. Chopra S, Foltz WD, Milosevic MF, Toi A, Bristow RG, Menard C, Haider MA (2009) Comparing oxygen-sensitive MRI (BOLD R2*) with oxygen electrode measurements: a pilot study in men with prostate cancer. *Int J Radiat Biol* 85(9):805–813
30. Hallac RR, Ding Y, Yuan Q, McColl RW, Lea J, Sims RD, Weatherall PT, Mason RP (2012) Oxygenation in cervical cancer and normal uterine cervix assessed using blood oxygenation level-dependent (BOLD) MRI at 3T. *NMR Biomed* 25(12):1321–1330
31. Li XS, Fan HX, Fang H, Song YL, Zhou CW (2015) Value of R2* obtained from T2*-weighted imaging in predicting the prognosis of advanced cervical squamous carcinoma treated with concurrent chemoradiotherapy. *J Magn Reson Imaging* 42(3):681–688
32. Olivero JJ, Longbothum RL (1977) Empirical fits to the Voigt line width: A brief review. *J Quant Spectrosc Radiat Transfer* 17(2):233–236
33. Armstrong BH (1967) Spectrum line profiles: The Voigt function. *J Quant Spectrosc Radiat Transfer* 7(1):61–88
34. Odicino F, Pecorelli S, Zigliani L, Creasman WT (2008) History of the FIGO cancer staging system. *Int J Gynaecol Obstet* 101(2):205–210
35. Gudbjartsson H, Patz S (1995) The Rician distribution of noisy MRI data. *Magn Reson Med* 34(6):910–914
36. Burnham KP, David RA (2002) Model selection and multimodel inference. A practical information-theoretic approach, 2nd edn. Springer-Verlag, New York
37. Bourne RM, Panagiotaki E, Bongers A, Sved P, Watson G, Alexander DC (2014) Information theoretic ranking of four models of diffusion attenuation in fresh and fixed prostate tissue ex vivo. *Magn Reson Med* 72(5):1418–1426
38. Stanisiz GJ, Odrobina EE, Pun J, Escaravage M, Graham SJ, Bronskill MJ, Henkelman RM (2005) T1, T2 relaxation and magnetization transfer in tissue at 3T. *Magn Reson Med* 54(3):507–512
39. Medved M, Chatterjee A, Devaraj A, Harmath C, Lee G, Yousuf A, Antic T, Oto A, Karczmar GS (2021) High spectral and spatial resolution MRI of prostate cancer: a pilot study. *Magn Reson Med* 86(3):1505–1513
40. Hernando D, Vigen KK, Shimakawa A, Reeder SB (2012) R*(2) mapping in the presence of macroscopic B(0) field variations. *Magn Reson Med* 68(3):830–840
41. Yang X, Sammet S, Schmalbrock P, Knopp MV (2010) Post-processing correction for distortions in T2* decay caused by quadratic cross-slice B0 inhomogeneity. *Magn Reson Med* 63(5):1258–1268

Publisher's Note Springer Nature remains neutral with regard to jurisdictional claims in published maps and institutional affiliations.

Springer Nature or its licensor holds exclusive rights to this article under a publishing agreement with the author(s) or other rightsholder(s); author self-archiving of the accepted manuscript version of this article is solely governed by the terms of such publishing agreement and applicable law.